# LETTER

Experimental realization of on-chip topological nanoelectromechanical metamaterials

Jinwoong Cha[1,2], Kun Woo Kim[3] & Chiara Daraio[2]*

Guiding waves through a stable physical channel is essential for reliable information transport. However, energy transport in high-frequency mechanical systems, such as in signal-processing applications[1], is particularly sensitive to defects and sharp turns because of back-scattering and losses[2]. Topological phenomena in condensed matter systems have shown immunity to defects and unidirectional energy propagation[3]. Topological mechanical metamaterials translate these properties into classical systems for efficient phononic energy transport. Acoustic and mechanical topological metamaterials have so far been realized only in large-scale systems, such as arrays of pendulums[4], gyroscopic lattices[5,6], structured plates[7,8] and arrays of rods, cans and other structures acting as acoustic scatterers[9–12]. To fulfil their potential in device applications, mechanical topological systems need to be scaled to the on-chip level for high-frequency transport[13–15]. Here we report the experimental realization of topological nanoelectromechanical metamaterials, consisting of two-dimensional arrays of free-standing silicon nitride nanomembranes that operate at high frequencies (10–20 megahertz). We experimentally demonstrate the presence of edge states, and characterize their localization and Dirac-cone-like frequency dispersion. Our topological waveguides are also robust to waveguide distortions and pseudospin-dependent transport. The on-chip integrated acoustic components realized here could be used in unidirectional waveguides and compact delay lines for high-frequency signal-processing applications.

Nanoelectromechanical systems[16,17] can be employed to build on-chip topological acoustic devices, thanks to their ability to transduce electrical signals into mechanical motion, which is essential in applications. Moreover, nonlinear dynamic phenomena are easily accessible in nanoelectromechanical devices. For example, previous
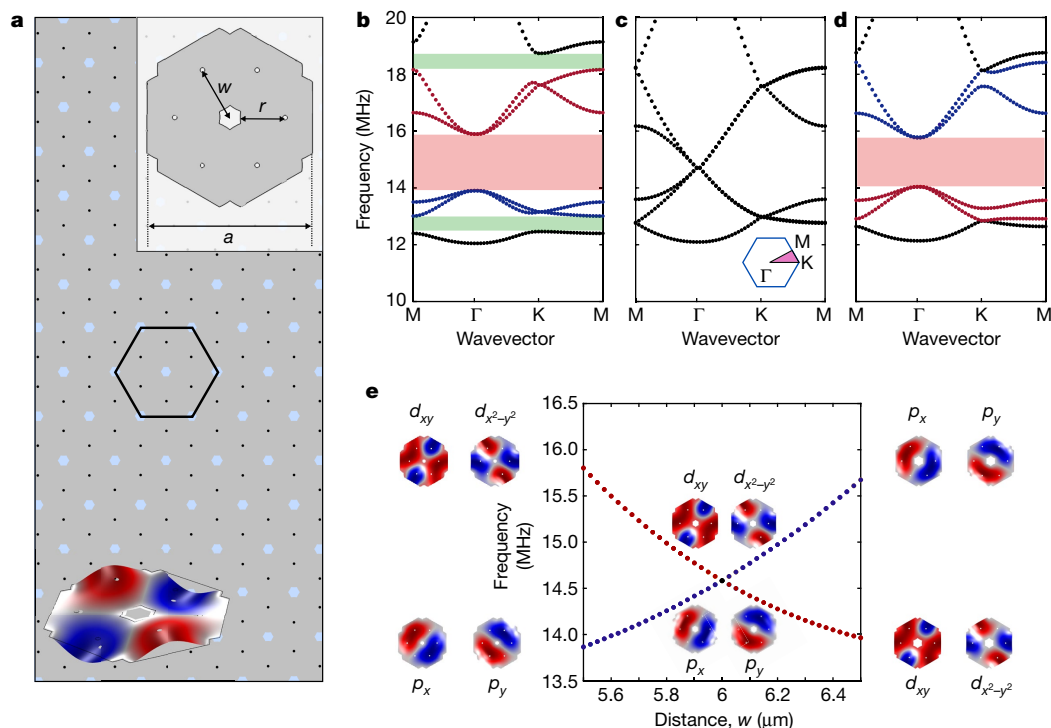
Fig. 1 | Unit cell geometry and topological phase transitions. a, Schematic of a two-dimensional NEMM. The grey area represents the SiN nanomembrane suspended over a highly doped n-type silicon substrate. The black dots, forming a honeycomb lattice, represent etch holes. The light-blue hexagons represent the unetched thermal oxide, acting as fixed boundaries. The unit cell geometry (black solid hexagon) is shown in the right inset, with relevant parameters. An example flexural mode is shown in the left inset. The topological phases are controlled by changing the centre-to-hole distance w. r denotes the radius of the etching path from the etch holes.

b–d, Frequency dispersion curves along a boundary of the irreducible Brillouin zone MΓKM, for $w = 5.5\,\mu m$ (**b**), $6.0\,\mu m$ (**c**) and $6.5\,\mu m$ (**d**); $r = 4.9\,\mu m$. The red- and green-shaded regions correspond to topological and non-topological bandgaps, respectively. **e**, Eigenfrequencies above and below the topological bandgap at the Γ point, as a function of w. Blue (red) dots denote the eigenfrequencies for flexural modes p_x and p_y (d_{xy} and $d_{x^2-y^2}$). The flexural mode shapes are presented for $w = 5.5\,\mu m$ (left), $6.0\,\mu m$ (middle) and $6.5\,\mu m$ (right).

[1]Department of Mechanical and Process Engineering, ETH Zurich, Zurich, Switzerland. [2]Engineering and Applied Science, California Institute of Technology, Pasadena, CA, USA. [3]Korea Institute for Advanced Study, Seoul, South Korea. *e-mail: daraio@caltech.edu
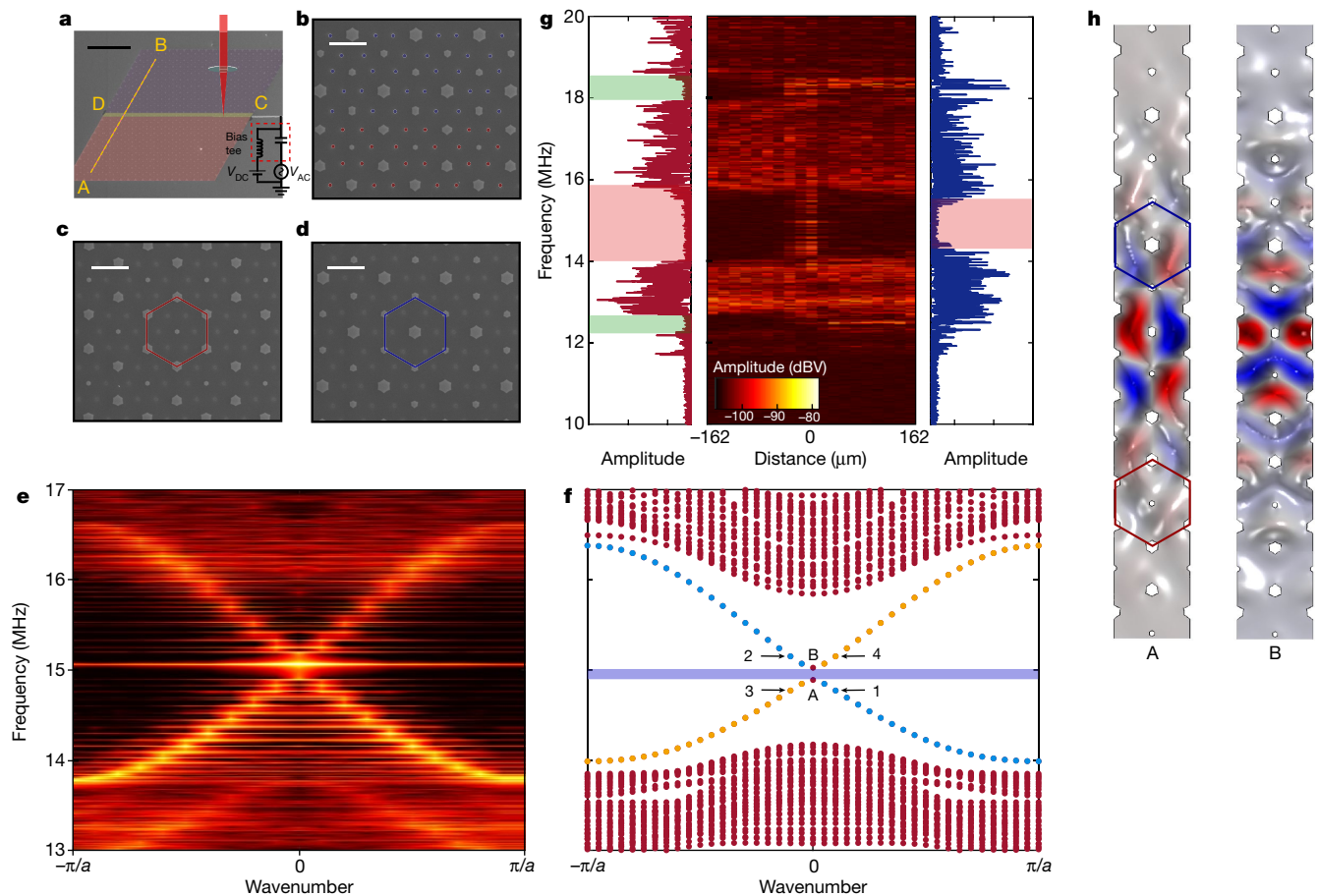
Fig. 2 | Characterization of topological edge states. a, Scanning electron microscope (SEM) image of a straight topological edge waveguide. The two different topological phases are fasle-colour-shaded in blue (non-trivial) and red (trivial). Flexural membrane motions are excited by simultaneously applying a constant and alternating voltages (V_{DC} = 2 V, V_{AC} = 20 mV) to the excitation electrode via a bias tee. Scale bar, 100 μm. **b–d**, SEM images of an edge region (**b**; the yellow-shaded strip C–D in **a**) a trivial lattice with w = 5.5 μm (**c**; the red-shaded area in **a**) and a non-trivial lattice with w = 6.5 μm (**d**; the blue-shaded area in **a**). Scale bars, 10 μm. The red and blue dots in **b** denote the lattice points for w = 5.5 μm and w = 6.5 μm, respectively. The red (**c**) and blue (**d**) hexagons represent the unit cells for w = 5.5 μm and w = 6.5 μm, respectively. **e, f**, Experimental (**e**) and numerical (**f**) frequency dispersion curves along the edge waveguide (C–D in **a**). Yellow and light-blue dots in the edge-state dispersion in **f** represent propagating waves for two opposite pseudospins. Time evolutions of the mode shapes at points 1, 2, 3 and 4 are provided in Supplementary Videos 1–4. **g**, Frequency responses for 19 different sites along the yellow dashed line A–B in **a** (middle panel). The left and right panels represent frequency responses at sites A and B, respectively. The red- and green-shaded regions represent the bandgaps. **h**, Flexural modes for points A and B in the dispersion shown in **f**. The width of the strip is 18 μm, identical to the lattice parameter a.

studies of systems with few degrees of freedom have demonstrated quantum-analogous phenomena, like cooling and amplification[18], and Rabi oscillation[19,20]. One-dimensional nanoelectromechanical lattices are a different class of nanoelectromechanical devices used to study lattice dynamics, for example, in waveguiding[21–23] and energy focusing[24]. Recently, one-dimensional nanoelectromechanical lattices made of SiN nanomembranes have demonstrated active manipulation of phononic dispersion, leveraging electrostatic softening effects and nonlinearity[23].

To design our topological nanoelectromechanical metamaterial (NEMM), we implemented the well known extended honeycomb lattice scheme[25]. The approach emulates electronic topological insulators for bosonic excitations in metamaterials. The extended honeycomb lattice contains six sites in a unit cell, satisfying C_6 crystalline symmetry[25]. This is an effective design strategy for device applications because of its geometrical simplicity. This lattice exploits Brillouin-zone folding to demonstrate a double-Dirac cone at the Γ point of the Brillouin zone. This zone-folding method has recently been used in various topological elastic[8,15], acoustic[9,11] and photonic[25,26] systems, by introducing the concept of pseudospins that satisfy Kramers theorem[3]. Brillouin-zone folding allows us to realize a pseudotime-reversal-symmetry-invariant system, where an anti-unitary, pseudotime-reversal operator U_T (where $U_T U_T^\dagger = -I$) is defined from the crystalline symmetry (C_6) of the lattice[25]. Despite the practicality of the structure, the consequent

topological edge states are robust only against defects that preserve local C_6 symmetry, which is an inevitable drawback of crystalline-symmetry-based designs.

We realize these topological properties in our NEMM by periodically arranging etch holes, of diameter 500 nm, in an extended honeycomb lattice (Fig. 1a). The etch holes enable a buffered oxide etchant to partially remove the sacrificial thermal oxide layer and release the SiN suspended membranes (Extended Data Fig. 1). We engineer the topological phases of the lattice by changing the distance between etch holes, w (Fig. 1a). Our NEMM consequently forms a flexural phononic crystal, consisting of a periodic array of free-standing SiN nanomembranes. The average thickness of the nanomembranes is about 79 nm. The average vacuum gap distance between the SiN layer and the highly doped silicon substrate is about 147 nm. These values are estimated considering the partial etching rate of the SiN in the buffered oxide etchant (about 0.3 nm min^{-1}).

We perform finite element simulations using COMSOL Multiphysics (https://www.comsol.com/), to numerically compute frequency dispersion curves for a unit cell with a lattice parameter a = 18 μm (Extended Data Fig. 2). We vary the distance between two neighbouring holes, w, from 5.5 μm to 6.5 μm (Fig. 1b, e). For a unit cell with w = 6.0 μm = $a/3$, a double Dirac cone is present around 14.55 MHz at the Γ point of the Brillouin zone (Fig. 1c). The frequency dispersion curves typically start
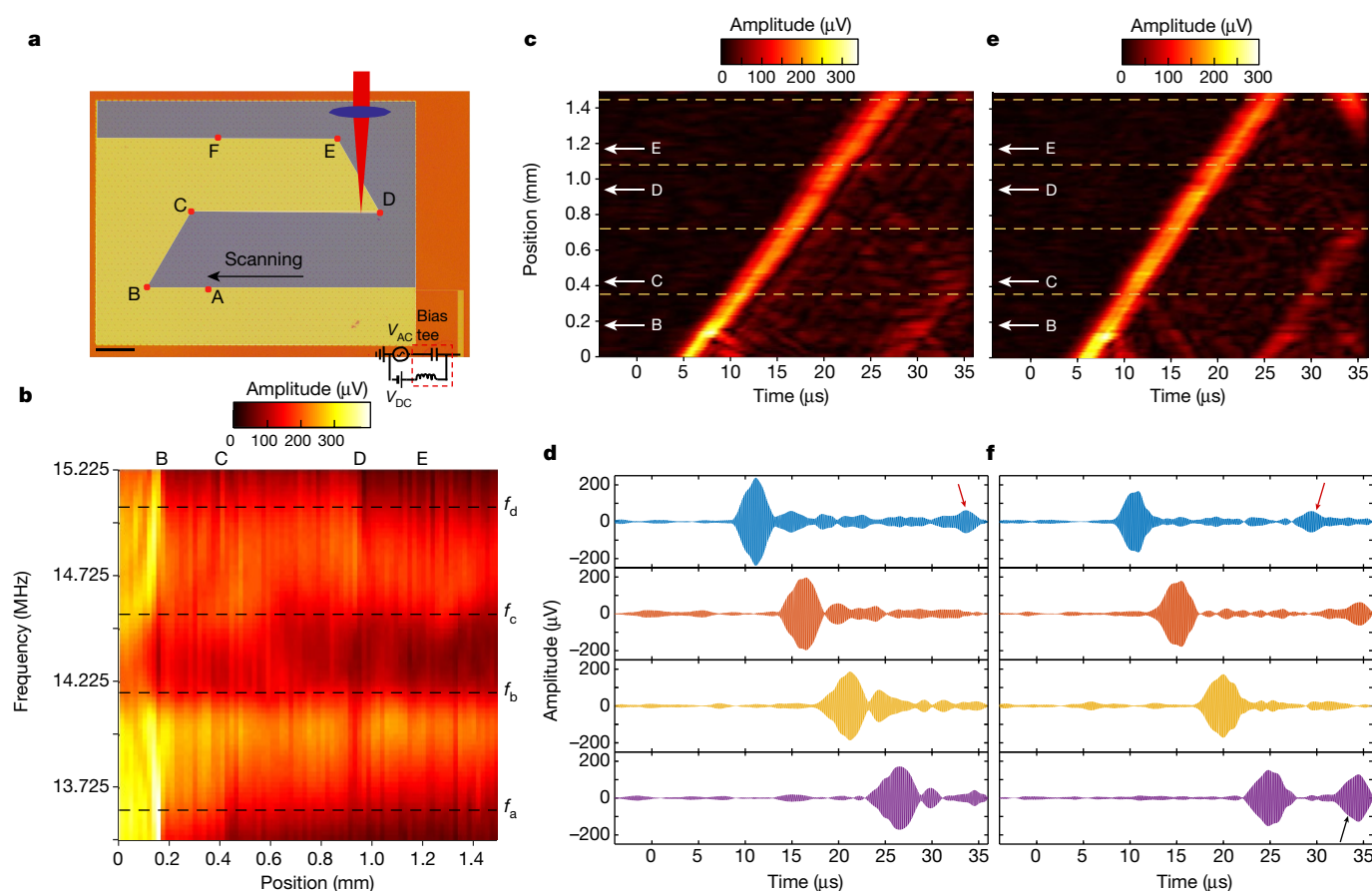
Fig. 3 | Waveguide robustness against imperfections. a, Optical microscope image of a zigzag topological edge waveguide. The blue- and yellow-shaded regions represent topologically trivial and non-trivial lattices, respectively. Time-domain responses are measured along the edge waveguide from points A to F. Points B, C, D and E denote the corners. The flexural membrane motions are excited by simultaneously applying a constant and a chirped voltage signal with frequencies ranging from 12.8 MHz to 15.8 MHz. The applied voltages are $V_{DC} = 15$ V and $V_P = 30$ mV, where V_P is the amplitude of the chirped signal. Scale bar, 100 μm. **b**, The colour scale represents the amplitudes from wavelet analyses at different positions of the edge waveguide. The frequencies ranging from f_a to f_b and from f_c to f_d represent propagating edge states. **c, e**, Spatiotemporal responses along the edge waveguide in a space–time domain. Pulses with centre frequencies of 13.85 MHz (**c**) and 14.75 MHz (**e**) and a bandwidth of 0.3 MHz are considered. **d, f**, Time-domain responses for pulses with centre frequencies of 13.85 MHz (**d**) and 14.75 MHz (**f**) at the 20th (blue), 40th (red), 60th (yellow) and 80th (purple) unit cells along the edge waveguide, which are highlighted with yellow-dashed lines in **c** and **e**. The red (black) arrow indicates the reflected pulse from the input (output) boundary.

from around 12 MHz, because of the presence of clamped boundaries. The frequency dispersion curves for $w = 5.5$ μm and 6.5 μm show the emergence of approximately 1.8-MHz-wide band gaps at the Γ point, ranging from 14 MHz to 15.8 MHz. The lattice with $w = 5.5$ μm exhibits two additional bandgaps below and above the centre bandgap around 15 MHz (Fig. 1b), while the lattice with $w = 6.5$ μm (Fig. 1d) does not. The four vibrational modes, p_x, p_y, d_{xy} and $d_{x^2-y^2}$, at the Γ point are degenerate at the Dirac point for the lattice with $w = 6$ μm (Fig. 1c, e). The four degenerate modes are split into two separate degenerate modes, for $w < 6$ μm and $w > 6$ μm (Fig. 1e), opening a bandgap. The band inversion between the dipole vibrational modes (p_x, p_y) and the quadrupole ones (d_{xy}, $d_{x^2-y^2}$) appears at the Γ point for $w > 6$ μm, which supports the topological non-triviality of the lattice. To confirm the presence of the pseudospins, we derive a Hamiltonian matrix for pseudospin states $p_\pm = p_x \pm ip_y$ and $d_\pm = d_{x^2-y^2} \pm id_{xy}$ around the Γ point (Methods). We apply the **k·p** perturbation method (see Methods) to the wave equation for a thin plate, $D\nabla^4 W = -\rho h(\partial^2 W/\partial t^2)$, and show the similarity with the Bernevig–Hughes–Zhang model for CdTe/HgTe/CdTe quantum wells[27].

To investigate the topological properties of our NEMMs experimentally, we fabricate a straight topological edge waveguide (Fig. 2a, b), formed at the interface of the topologically trivial ($w = 5.5$ μm, Fig. 2c) and non-trivial ($w = 6.5$ μm, Fig. 2d) lattices. Topological edge states do not exist at free boundaries of our systems, owing to the lack of C_6 symmetry. The number of unit cells of each phase is approximately 200,

so that the edge waveguide has 20 supercells with 18-μm one-dimensional lattice spacing. To characterize the edge states, we excite the flexural motion of the membranes by applying a dynamic electrostatic force, $F \propto (V_{DC} + V_{AC})^2$, to the excitation electrode. Here, V_{DC} and V_{AC} are the constant and alternating voltages, which are simultaneously applied between the excitation electrode and the grounded substrate (Fig. 2a). We perform measurements using a home-built Michelson interferometer with a balanced homodyne detection scheme (Methods). To obtain the dispersion curves of the edge states, we measure the frequency responses of 20 sites along the edge waveguide, by spatially scanning the measurement points (yellow strip, Fig. 2a) with 18-μm steps (Extended Data Fig. 3). The Dirac-like edge-state frequency dispersion curves, isolated from the bulk dispersion, are present in the frequency range 14.1–15.8 MHz, showing good agreement with the numerical dispersion curves (Fig. 2f). We also observe a defect mode at the crossing point of the edge-state dispersion curves (Fig. 2e). This stems from a point-defect mode at the boundary near the excitation region (Extended data Fig. 4a). The broken C_6 symmetry at the interface (Fig. 2b) induces a small bandgap in the middle of the edge-state dispersions (Fig. 2e, f). Despite the presence of the bandgap, the defect mode is allowed to transmit non-negligible energy to the end of the waveguide owing to the long decay length of the evanescent mode (Extended data Fig. 4b).

We also characterize the localization of the edge states, by scanning the measurement point across the waveguide (yellow dashed line A–B
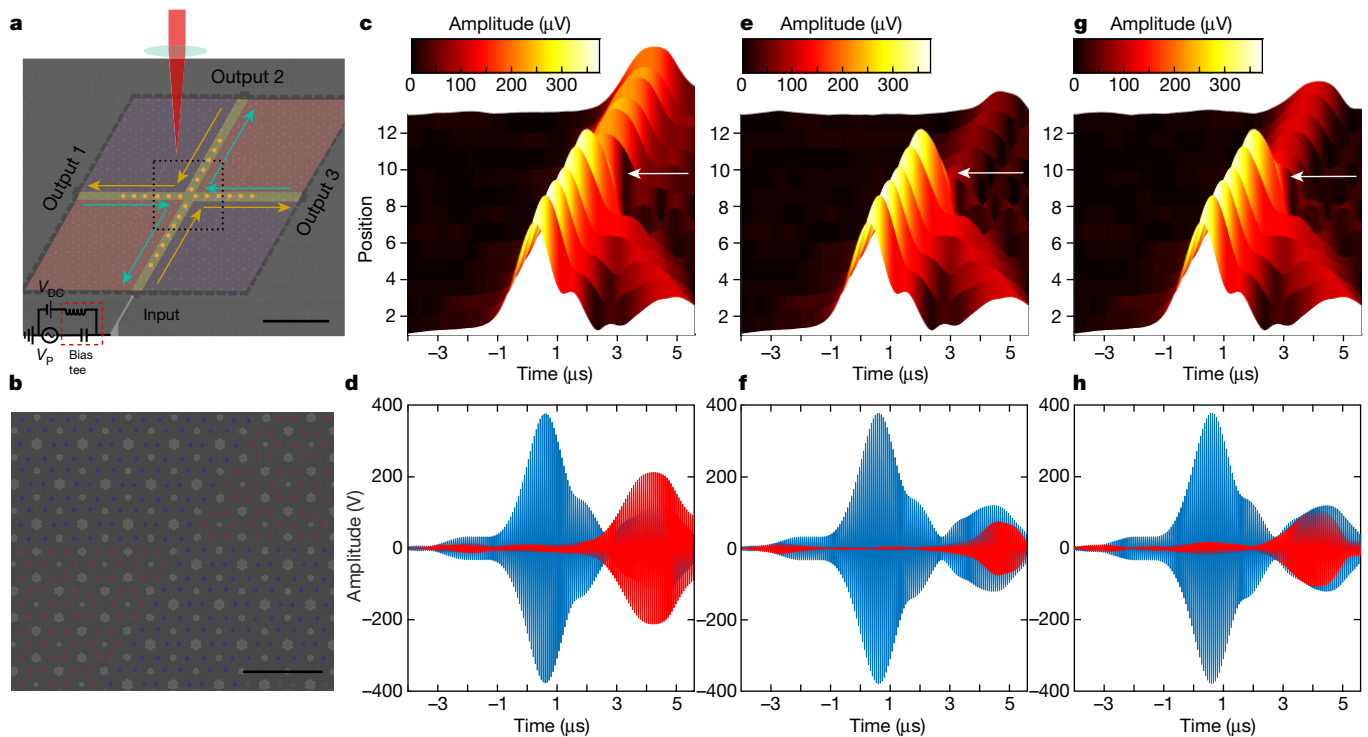
Fig. 4 | Pseudospin-dependent wave propagation. a, SEM image of a pseudospin-filter configuration. Scale bar, 100 μm. The two different topological phases are false-colour-shaded in red (trivial, $w = 5.5$ μm) and blue (non-trivial, $w = 6.5$ μm). Flexural motions are excited from the electrode ($V_{DC} = 15$ V, $V_P = 22.5$ mV). The yellow and cyan arrows represent propagating directions for different pseudospin states. **b**, Close-up view of the region marked by the dotted square in **a**. The red and blue dots denote the lattice points for trivial and non-trivial phases.

Scale bar, 30 μm. **c, e, g**, Envelopes of propagating pulses (15.2-MHz centre frequency, 0.5-MHz bandwidth) in the space–time domain. The position represents the measurement points along the edge waveguides. **c**, Input to output port 1; **e**, input to output port 2; and **g**, input to output port 3. The crossing points are indicated by white arrows. **d, f, h**, Time-domain responses of the propagating pulses at position 1, input side (blue) and position 13, output side (red). **d**, Output port 1; **f**, output port 2; and **h**, output port 3.

in Fig. 2a), also with 18-μm steps. The edge states are strongly localized (Fig. 2h) within ±36 μm from the interface (Fig. 2g). Beyond this range, the frequency responses (Fig. 2g) start to show clear bandgaps, with frequency ranges and widths similar to the numerical dispersion relations shown in Fig. 1b and d. The trivial lattice presents three bandgaps (Fig. 2g, left) and the non-trivial lattice shows only one topological bandgap (Fig. 2g, right), as predicted by the numerical frequency dispersion (Fig. 1b–d). The frequency responses show evidence of different topological phases in the two lattices, with $w = 5.5$ μm and 6.5 μm, confirming that the waveguiding effect is topological.

One remarkable feature of topological edge modes is their robustness to waveguide imperfections, such as sharp corners. To study this, we fabricate a long, distorted edge waveguide that includes four corners with two 60° and two 120° angles (Fig. 3a). This waveguide consists of 134 unit cells. We perform steady-state measurements (Methods) and confirm the presence of the topological edge states (Extended Data Fig. 5a). The bandgap of the trivial phase is observed in the range 13.7–15.1 MHz and that for the non-trivial phase in the range 13.7–14.8 MHz. To confirm immunity to back-scattering, we measure transient responses of propagating pulses over 84 unit cells along the edge waveguide (points A to F in Fig. 3a). We excite chirped signals with frequencies ranging from 12.8 MHz to 15.8 MHz (Methods). The propagating pulses that correspond to the edge states (frequencies of 13.7–14.1 MHz and 14.5–14.9 MHz) exhibit small-amplitude decays despite the presence of the corners (Fig. 3b). To closely examine the propagating pulses, we select two pulses whose centre frequencies (13.85 MHz in Fig. 3c and 14.75 MHz in Fig. 3e) lie in the lower and upper edge states with respect to the small bandgap around 14.3 MHz. The propagation speeds extracted from the data are 69.1 m s⁻¹ (for the 13.85-MHz pulse) and 78.6 m s⁻¹ (for the 14.75-MHz pulse). We note that the waves propagate along the entire length of the edge waveguide without visible leakage in the bulk from the excitation point (Fig. 3c, e) and with little

backscattering from the corners (Fig. 3c–f). This confirms that the energy transport is very stable and strongly confined at the interface. The low backscattering and signal decay may be attributable to scattering of the parasitic bulk modes (which coexist with the edge modes) as well as to partial pseudospin-mode conversion due to imperfect C_6 symmetry at the corners. The ability to introduce sharp corners (as in B, C, D and E) allows longer waveguides (for example, in delay lines) to be designed within the same device size.

Another crucial aspect of topological insulators is unidirectional propagation for distinct pseudospin modes. To characterize this, we fabricate another NEMM with a spin-splitter configuration consisting of four domain walls that has been employed in several previous studies[11,12] (Fig. 4a, b). Such geometry allows us to use a simpler pseudospin selective excitation. We send voltage pulses to the excitation electrode and measure transient responses of the propagating pulses (Methods). We scan 13 sites (7 sites from the input channel and 6 sites from each output channel) near the crossing point of the channels (Fig. 4b). Note that the steady-state frequency responses at the end of the three output ports (Fig. 4a) exhibit almost identical edge-state responses owing to boundary scattering (Extended Data Fig. 6b–d). The pulse we investigate has a 15.1-MHz centre frequency and 0.5-MHz bandwidth, which is enough to cover the broad frequency ranges of edge states. In this configuration, the propagating direction of a pseudospin state depends on the spatial configuration of the two topological phases, $w = 5.5$ μm and 6.5 μm (Fig. 4a). The pseudospin states are filtered to have a single dominant state in the input port (yellow arrow in Fig. 4a). After the signal passes the input channel, the filtered spin state mainly propagates to output port 1 and 3 (yellow arrows in Fig. 4a) as shown in Fig. 4c, d, g and h. The edge state leading to port 2 supports pseudospin modes that are opposite to the input modes in the propagation direction (cyan arrow, Fig. 4a). As such, we would expect no signal to reach port 2. However, we observe a small, but visible energy propagation (Fig. 4e, f).

This unexpected penetration might arise from the partial conversion of pseudospin modes at the centre crossing point, where the C_6 symmetry is broken. Nonetheless, the results confirm that the propagation direction depends on the type of pseudospin. The use of spin-selective excitation and detection methods will enable the realization of compact, mechanical unidirectional components.

Here we have demonstrated scalable and reliable on-chip devices that support two-dimensional topological phenomena. These phenomena can be employed for stable and compact ultrasound and radio-frequency signal processing. With advanced nanofabrication techniques, more sophisticated structures can be realized to design other types of topological device, based on perturbative metamaterials design methods, for example[7,28]. Moreover, frequency tunability in nanoelectromechanical resonators via electrostatic forces[29,30] will be of use in electrically tunable devices[23] and actively reconfigurable topological channels[31].

Online content

Any methods, additional references, Nature Research reporting summaries, source data, statements of data availability and associated accession codes are available at https://doi.org/10.1038/s41586-018-0764-0.

1. Olsson, R. H. III & El-Kady, I. Microfabricated phononic crystal devices and applications. *Meas. Sci. Technol.* **20**, 012002 (2009).
2. Baboly, M. G. et al. Demonstration of acoustic waveguiding and tight bending in phononic crystals. *Appl. Phys. Lett.* **109**, 183504 (2016).
3. Hasan, M. Z. & Kane, C. L. Topological insulators. *Rev. Mod. Phys.* **82**, 3045–3067 (2010).
4. Süsstrunk, R. & Huber, S. D. Observation of phononic helical edge states in a mechanical topological insulator. *Science* **349**, 47–50 (2015).
5. Nash, L. M. et al. Topological mechanics of gyroscopic metamaterials. *Proc. Natl Acad. Sci. USA* **112**, 14495–14500 (2015).
6. Mitchell, N. P., Nash, L. M., Hexner, D., Turner, A. M. & Irvine, W. T. M. Amorphous topological insulators constructed from random point sets. *Nat. Phys.* **14**, 380–385 (2018).
7. Serra-Garcia, M. et al. Observation of a phononic quadrupole topological insulator. *Nature* **555**, 342–345 (2018).
8. Yu, S. et al. Elastic pseudospin transport for integratable topological phononic circuits. *Nat. Commun.* **9**, 3072 (2018).
9. He, C. et al. Acoustic topological insulator and robust one-way sound transport. *Nat. Phys.* **12**, 1124–1129 (2016).
10. Lu, J. et al. Observation of topologically valley transport of sound in sonic crystals. *Nat. Phys.* **13**, 369–374 (2017).
11. Yves, S., Fleury, R., Lemoult, F., Fink, M. & Lerosey, G. Topological acoustic polaritons: robust and sound manipulation at the subwavelength scale. *New J. Phys.* **19**, 075003 (2017).
12. He, H. et al. Topological negative refraction of surface acoustic waves in a Weyl phononic crystal. *Nature* **560**, 61–64 (2018).
13. Peano, V., Brendel, C., Schmidt, M. & Marquardt, F. Topological phases for sound and light. *Phys. Rev. X* **5**, 031011 (2015).
14. Brendel, C., Peano, V., Painter, O. J. & Marquardt, F. Pseudomagnetic fields for sound at the nanoscale. *Proc. Natl Acad. Sci. USA* **114**, E3390–E3395 (2017).
15. Brendel, C., Peano, V., Painter, O. J. & Marquardt, F. Snowflake phononic topological insulator at the nanoscale. *Phys. Rev. B* **97**, 020102 (2018).
16. Huang, X. M. H., Zorman, C. A., Mehregany, M. & Roukes, M. L. Nanoelectromechanical systems: nanodevice motion at microwave frequencies. *Nature* **421**, 496 (2003).
17. Craighead, H. G. Nanoelectromechanical systems. *Science* **290**, 1532–1535 (2000).
18. De Alba, R. D. et al. Tunable phonon-cavity coupling in graphene membranes. *Nat. Nanotechnol.* **11**, 741–746 (2016).
19. Faust, T., Rieger, J., Seitner, M. J., Kotthaus, J. P. & Weig, E. M. Coherent control of a classical nanomechanical two-level system. *Nat. Phys.* **9**, 485–488 (2013).
20. Okamoto, H. et al. Coherent phonon manipulation in coupled mechanical resonators. *Nat. Phys.* **9**, 485–488 (2013).
21. Hatanaka, D., Mahboob, I., Onomitsud, K. & Yamaguchi, H. Phonon waveguides for electromechanical circuits. *Nat. Nanotechnol.* **9**, 520–524 (2014).
22. Hatanaka, D., Dodel, A., Mahboob, I., Onomitsud, K. & Yamaguchi, H. Phonon propagation dynamics in band-edngineered one-dimensional phononic crystal waveguides. *New J. Phys.* **17**, 113032 (2015).
23. Cha, J. & Daraio, C. Electrical tuning of elastic wave propagation in nanomechanical lattices at MHz frequencies. *Nat. Nanotechnol.* **13**, 1016–1020 (2018).
24. Kurosu, M., Hatanaka, D., Onomitsu, K. & Yamaguchi, H. On-chip temporal focusing of elastic waves in a phononic crystal waveguide. *Nat. Commun.* **9**, 1331 (2018).
25. Wu, L. & Hu, X. Scheme for achieving a topological photonic crystal by using dielectric material. *Phys. Rev. Lett.* **114**, 223901 (2015).
26. Yves, S. et al. Crystalline metamaterials for topological properties at subwavelength scales. *Nat. Commun.* **8**, 16023 (2017).
27. Bernevig, B. A., Hughes, T. L. & Zhang, S. C. Quantum spin Hall effect and topological phase transition in HgTe quantum wells. *Science* **314**, 1757–1761 (2006).
28. Matlack, K. H., Serra-Garcia, M., Palermo, A., Huber, S. D. & Daraio, C. Designing perturbative metamaterials from discrete models. *Nat. Mater.* **17**, 323–328 (2018).
29. Chen, C. et al. Graphene mechanical oscillators with tunable frequency. *Nat. Nanotechnol.* **8**, 923–927 (2013).
30. Bagci, T. et al. Optical detection of radio waves through a nanomechanical transducer. *Nature* **507**, 81–85 (2014).
31. Cheng, X. et al. Robust reconfigurable electromagnetic pathways within a photonic topological insulator. *Nat. Mater.* **15**, 542–548 (2016).

METHODS

Sample fabrication. The fabrication process begins with a pattern transfer by electron beam lithography and development of a PMMA resist in a MIBK:IPA = 1:3 solution. The excitation electrodes, made of a Au (45 nm)/Cr (5 nm) layer, are deposited on a 100-nm-LPCVD (low-pressure chemical vapour deposition) silicon nitride (SiN_x)/140-nm thermal SiO_2/525-μm highly doped Si wafer, followed by a lift-off process in acetone. A second electron beam lithography step, with ZEP 520A electron-beam resist, is then performed to create the pattern of etch holes (with diameter 500 nm) arranged in the extended honeycomb lattices (Fig. 1a and Extended Data Fig. 1). We use an ICP-reactive ion etch, to drill the holes on the SiN_x layer. After we finish the etching of the holes, we immerse the samples in a buffered oxide etchant solution for about 45–46 min, to partially etch the thermal SiO_2 underneath the SiN_x device layer. The etching duration determines the diameter of the etching circles, r (Extended Data Fig. 1). Detailed fabrication methods can be found in ref. [23]. Different samples were fabricated for the measurements in Figs. 2 and 3, with slightly different etching times. These differences in fabrication lead to a small change in the operating frequencies.

Experiments. The flexural motions of the membranes are measured using a homebuilt optical interferometer (HeNe laser, wavelength 633 nm) with a balanced homodyne method. The measurements are performed at room temperature and a vacuum pressure of $p < 10^{-6}$ mbar. The optical path length difference between the reference and the sample arms is stabilized by actuating a reference mirror. This mirror is mounted on a piezoelectric actuator that is controlled by a proportional integral derivative (PID) controller. The motion of the membranes is electrostatically excited by simultaneously applying a constant and a time-varying voltage through a bias tee (Mini-circuits, ZFBT-6GW+). The intensity of the interfered light from the reference mirror and the sample is measured using a balanced photodetector, which is connected to a high-frequency lock-in amplifier (Zurich instruments, UHFLI). The measurement position, monitored via a complementary metal–oxide–semiconductor (CMOS) camera, can be controlled by moving a vacuum chamber mounted on a motorized XY linear stage.

For the dispersion curve measurements in Fig. 2 and in the Extended Data Fig. 5, we measure (at steady-state) frequency responses of 10–20 MHz of 20 scanned sites along the edge waveguide. The scanning step is the one-dimensional lattice spacing, $a = 18$ μm. The lock-in amplifier (Zurich instruments, UHFLI) allows us to measure the amplitude responses and the phase differences between the measured signal and the excitation source. To plot the frequency dispersion, we perform fast Fourier transformation of the amplitude × sin(phase) data. The amplitude-only data and the phase-considered data are shown in Extended Data Fig. 3a and b.

For transient measurements in Figs. 3 and 4, we send a chirped signal (AWG module in UHFLI) and measure the signal with an oscilloscope (Tektronix, DPO3034). As the signal is invisible for a low-excitation amplitude, we first filter the radio-frequency output signals from the photodetector with a passive band-pass filter (6–22 MHz bandwidth) and an average of 512 datasets in the time-domain. For robustness measurements (Fig. 3), we send a pulse containing frequency content ranging from 12.8 MHz to 15.8 MHz, by applying $V_{DC} = 15$ V and $V_P = 30$ mV to the excitation electrode. We then perform post-signal processing to extract signals of interest, by applying a Burtterworth filter for different centre frequencies with 0.3-MHz bandwidth. For pseudospin-dependent transport measurements, we use a pulse (14–16 MHz) and applied $V_{DC} = 15$ V and $V_P = 22.5$ mV. We apply a Burtterworth filter with 15.2-MHz centre frequency and 0.5-MHz bandwidth.

Numerical simulations. We perform finite-element simulations to calculate the phononic frequency dispersion curves using COMSOL multiphysics. We employ the pre-stressed eigenfrequency analysis module in membrane mechanics. We also consider geometric nonlinearity, to reflect the effects of residual stresses. The physical properties of SiN_x used in the simulations are density 3,000 kg m^{-3}, Young's modulus 290 GPa, Poisson ratio 0.27 and isotropic in-place residual stress 50 MPa. The lattice parameter, a, is chosen to be 18 μm. We calculate frequency dispersion curves for various unit cell geometries with different w ranging from 5.5 μm to 6.5 μm. The centre hexagon and the six corners of each unit cell are fixed, owing to the presence of unetched SiO_2 (light-grey regions in the SEM images in Fig. 2b–d). The radii of the etched circles are set to $r = 4.9$ μm (Fig. 1 and Extended Data Fig. 2). We apply Bloch periodic conditions to the six sides of a unit cell, $u(\mathbf{r} + \mathbf{R}) = u(\mathbf{r})\exp(i\mathbf{q} \cdot \mathbf{R})$, via Floquet periodicity in COMSOL. Here, $u(\mathbf{r})$ is a periodic displacement function, $\mathbf{r}$ is a position within a unit cell, $\mathbf{R}$ is a lattice translation vector, and $\mathbf{q}$ is a wavevector. We calculate the dispersion curves along the boundary of the irreducible Brillouin zone ΔMΓK in Fig. 1c.

We also numerically calculate the frequency dispersion curves of the edge states to validate the topological behaviours. As we are interested in one-dimensional

dispersion along the interface, we build a strip-like super cell with 18-μm periodicity. Each topological phase ($w = 6.0 \pm 0.5$ μm) spans about ±160 μm from the interface in the direction perpendicular to the interface. We calculate the frequency dispersion by applying one-dimensional Bloch periodic conditions.

$k \cdot p$ perturbation method and Bernevig–Hughes–Zhang model. The equation of motion for a plate of thickness h is

$$D\nabla^4 W = -\rho h \frac{\partial^2 W}{\partial t^2}$$

Here, $D = Eh^3/[12(1 - \nu^2)]$ is the bending stiffness, ρ is density, h is the plate thickness and W is the plate displacement in the z direction. By inserting a Bloch function $W_{n,q}(\mathbf{r}) = e^{i(\mathbf{q}\cdot\mathbf{r} - \omega t)}Y_{n,q}(\mathbf{r})$ to the plate equation, we obtain $[D/(\rho h)]HY_{n,q} = \omega_{n,q}^2 Y_{n,q}$. Here, $\mathbf{r}$ is a position within a unit cell, $\mathbf{q}$ is a wavevector, n is a band index, $\omega_{n,q}$ is an eigenfrequency and $Y_{n,q}(\mathbf{r})$ is a periodic displacement function. The operator H is given by

$$H = \frac{\partial^4}{\partial x^4} + 2\frac{\partial^4}{\partial x^2 \partial y^2} + \frac{\partial^4}{\partial y^4}$$
$$+ |\mathbf{q}|^4 + 4i\mathbf{q}\cdot\boldsymbol{\nabla}(\nabla^2) - 4i|\mathbf{q}|^2\mathbf{q}\cdot\boldsymbol{\nabla} - 2|\mathbf{q}|^2\nabla^2 - 4\mathbf{q}\cdot\boldsymbol{\nabla}(\mathbf{q}\cdot\boldsymbol{\nabla})$$
$$= H^0 + H'(\mathbf{q})$$

The equation of motion that describes a plate vibration includes a square of the Laplacian operator ∇^4, so the higher-order wavevector terms arise, accordingly. Here, we consider the $\mathbf{q}$-dependent terms, $H'(\mathbf{q})$, as a small perturbation, as we are only interested in the behaviours near the Γ point ($\mathbf{q} = \mathbf{0}$) of the Brillouin zone. This perturbation term is equivalent to the $k \cdot p$ term in the $k \cdot p$ perturbation theory in quantum mechanics.

To obtain a Hamiltonian matrix on the pseudospin subspace, expressed in the basis $\{Y_{p_+,0}, Y_{d_+,0}, Y_{p_-,0}, Y_{d_-,0}\}$. We define the pseudospin states as $Y_{p_\pm,0} = (Y_{p_x,0} \pm iY_{p_y,0})/\sqrt{2}$ and $Y_{d_\pm,0} = (Y_{d_{x^2-y^2},0} \pm iY_{d_{xy},0})/\sqrt{2}$. The Bloch states, $Y_{p_x,0}, Y_{p_y,0}, Y_{d_{x^2-y^2},0}$ and $Y_{d_{xy},0}$, are the eigenstates of the operator at the Γ point. We neglect the cubic and quartic wavevector terms. The matrix elements can be calculated from

$$H_{n,m} = \oint_{\text{unit cell}} Y_{n,0}^* H^0 Y_{m,0}\,\mathrm{d}A$$
$$+ \oint_{\text{unit cell}} Y_{n,0}^*[4i\mathbf{q}\cdot\boldsymbol{\nabla}(\nabla^2) - 2|\mathbf{q}|^2\nabla^2 - 4\mathbf{q}\cdot\boldsymbol{\nabla}(\mathbf{q}\cdot\boldsymbol{\nabla})]Y_{m,0}\,\mathrm{d}A$$

where the indices n and m denote the pseudospin states. Neglecting the off-block-diagonal elements as they contribute as a higher-order perturbation, the matrix is expressed as

$$H(\mathbf{q}) = \alpha(\mathbf{q})I + \begin{bmatrix} \Omega(\mathbf{q}) & 0 \\ 0 & \Omega^*(-\mathbf{q}) \end{bmatrix}$$

where

$$\alpha(\mathbf{q}) = \frac{\omega_p^2 + \omega_d^2}{2} + \left(\frac{A+B}{2}\right)(q_x^2 + q_y^2)$$

$$\Omega(\mathbf{q}) = \begin{bmatrix} \frac{\omega_p^2 - \omega_d^2}{2} + \left(\frac{A-B}{2}\right)(q_x^2 + q_y^2) & C(q_x + iq_y) \\ C^*(q_x - iq_y) & -\left(\frac{\omega_p^2 - \omega_d^2}{2}\right) - \left(\frac{A-B}{2}\right)(q_x^2 + q_y^2) \end{bmatrix}$$

Here, the asterisk denotes the complex conjugate. The eigenvalues of H^0 are $\omega_p^2 = \omega_{p_x}^2 = \omega_{p_y}^2$ and $\omega_d^2 = \omega_{d_{x^2-y^2}}^2 = \omega_{d_{xy}}^2$. This matrix shows a similar form to the Hamiltonian matrix from Bernevig–Hughes–Zhang model[27] that describes the quantum spin Hall effect in two-dimensional systems. This result confirms that the system can support two different pseudospins.

Data availability

The data that support the findings of this study are available from the corresponding author upon reasonable request.

a

Etch holes

a

w

b

r

r

d

c

|	LPCVD SiN$_x$		Highly-doped Si
	Thermal SiO$_2$		Au/Cr
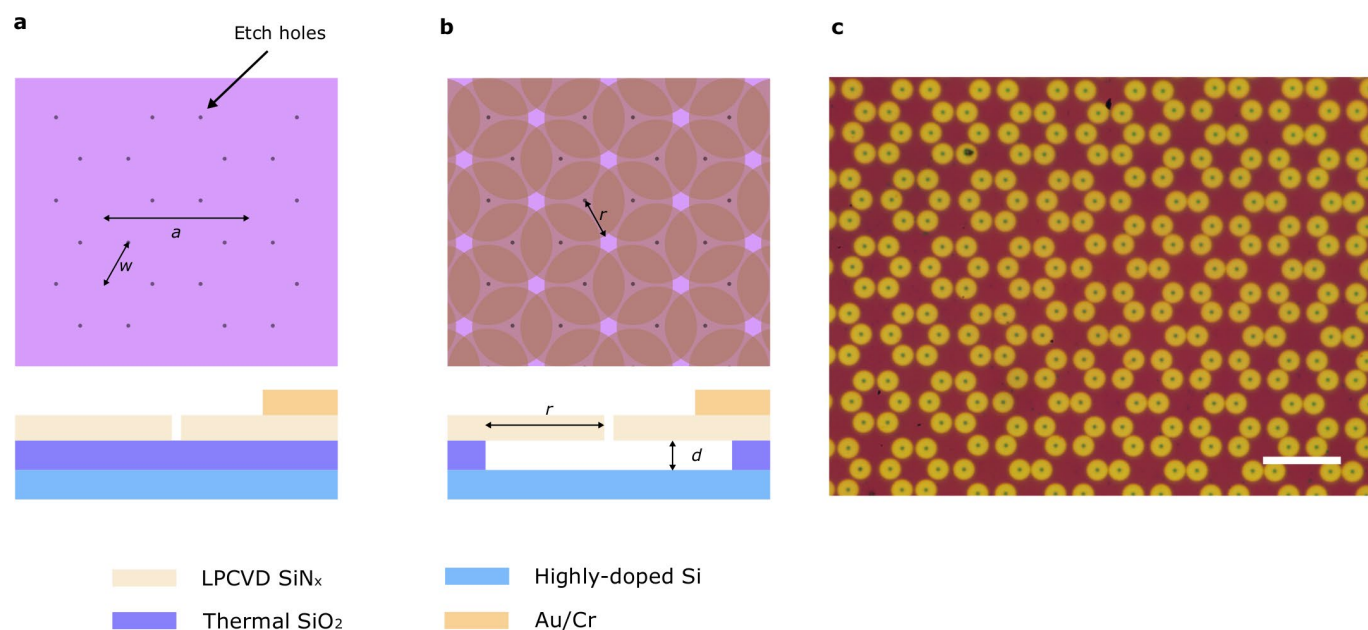
Extended Data Fig. 1 | Fabrication. a, Etch holes are periodically arranged in an extended honeycomb lattice. *a* is a lattice parameter and *w* is the distance between two neighbouring etch holes. The bottom picture shows the cross-sectional view. **b**, After a sample is immersed in a buffered oxide etchant, the thermal SiO$_2$ is radially etched from the etch holes. The etching paths are illustrated by the brown circles with radius *r*. The overlap between two membranes affects the coupling strength, by controlling the distance *w*. **c**, Optical microscope image of a partially etched samples. The yellow circles represent free-standing SiN$_x$ membranes and the darker/purple region is SiN$_x$/SiO$_2$. Scale bar, 18 μm.

a
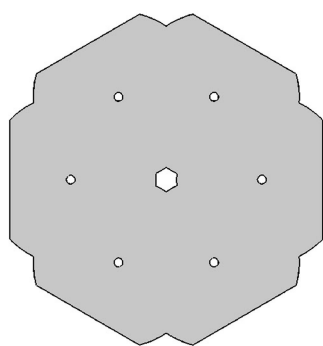
b
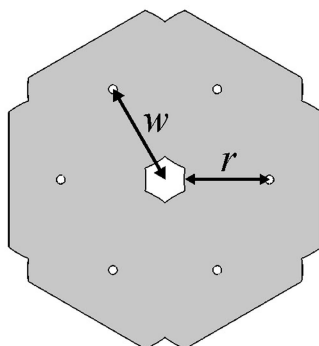
c
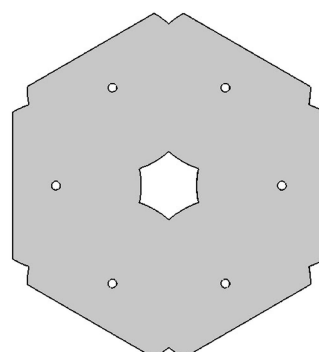
Extended Data Fig. 2 | Unit cell structures for the different topological phases. a–c, Unit cell geometries for $w = 5.5\,\mu m$ (**a**), $w = 6.0\,\mu m$ (**b**) and $w = 6.5\,\mu m$ (**c**). Here, $r = 4.9\,\mu m$ is the etching distance from the centre of the etch holes. The central hexagon and the six corners represent the regions of unetched thermal SiO_2. These are modelled as fixed boundaries in finite element simulations.
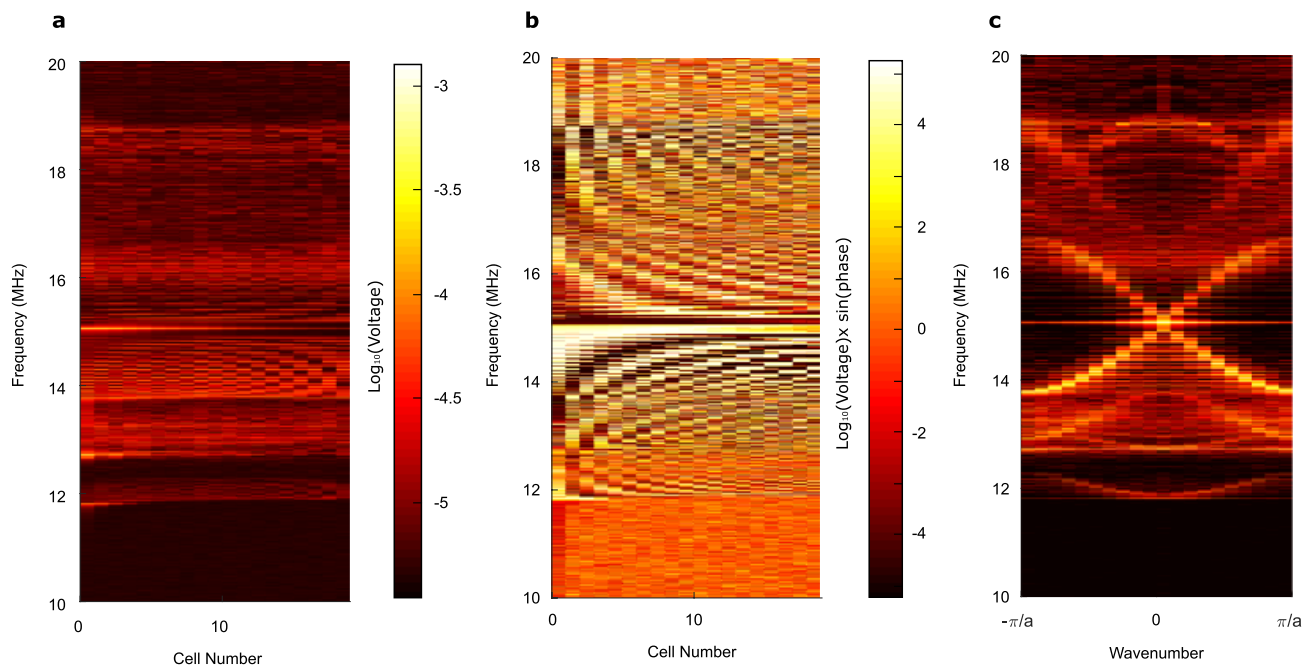
Extended Data Fig. 3 | Experimental characterization of the straight topological edge waveguide. a, Frequency responses (amplitude only) obtained from a spatial scan of 20 sites of the straight edge waveguide. The scanning period is 18 μm. The intensity decay around 15 MHz represents a defect mode. **b**, Amplitude × sin(phase) responses obtained from the spatial scan. **c**, Frequency dispersion obtained from Fourier transformation of the data shown in **b**.

a

b
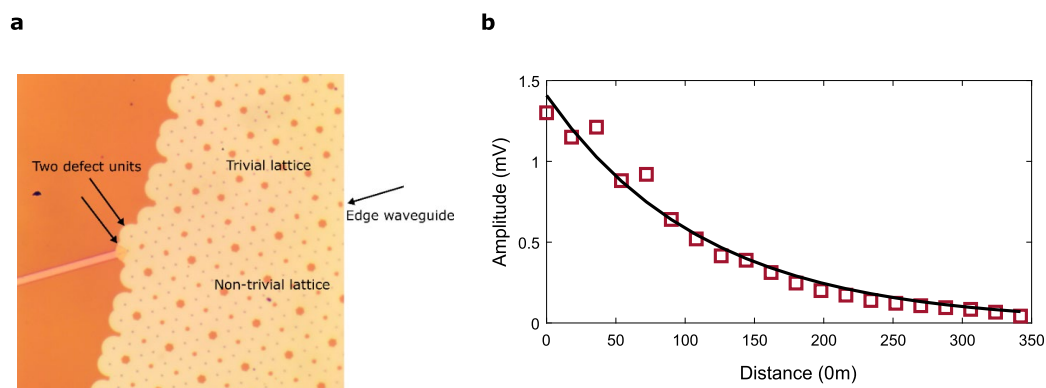
Extended Data Fig. 4 | Characteristics of the defect mode. a, Optical microscope image of the excitation region and the defective unit including the gold electrode. **b,** Experimental data for the amplitude decay of the defect mode. The red squares denote the experimental data and the black solid line represents a fitting function. Here, the fitting parameters a and b are 1.408 mV and 114.1292 μm.
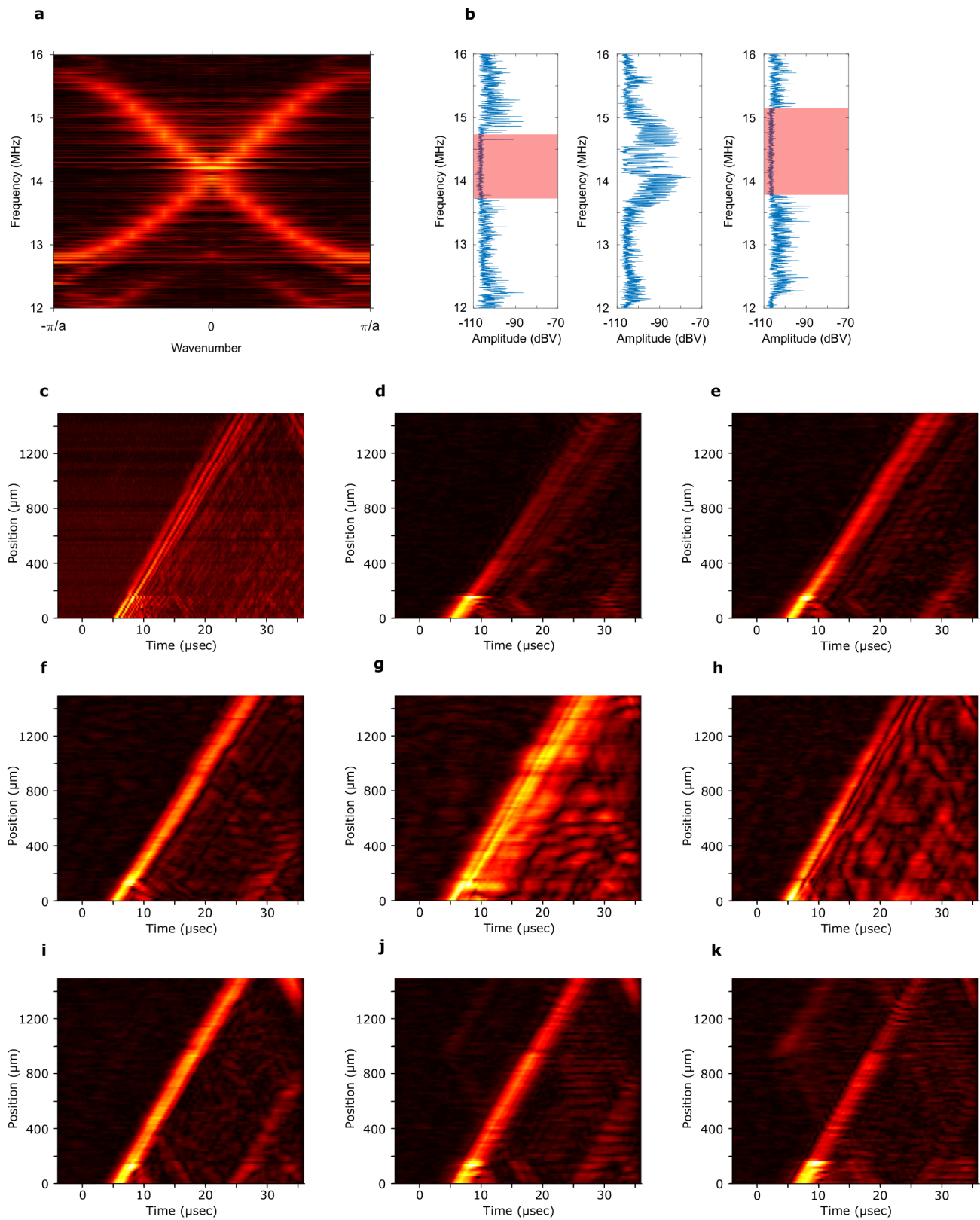
Extended Data Fig. 5 | Characteristics of the distorted waveguide.
a, Frequency dispersion curve along the edge waveguide. **b**, Frequency
responses of the bulk of the non-trivial phase (left), the output of the
edge waveguide (middle), and the bulk of the trivial phase (right).
c, A spatiotemporal response of unfiltered propagating pulses with
broadband frequencies ranging from 12.8 MHz to 15.8 MHz.

d–k, Filtered spatiotemporal responses of the propagating pulses with
different centre frequencies. The bandwidth of the pulses is 0.3 MHz. The
centre frequencies are 13.48 MHz (**d**), 13.68 MHz (**e**), 13.85 MHz (**f**),
14.1 MHz (**g**), 14.35 MHz (**h**), 14.75 MHz (**i**), 14. 975 MHz (**j**) and
15.23 MHz (**k**).
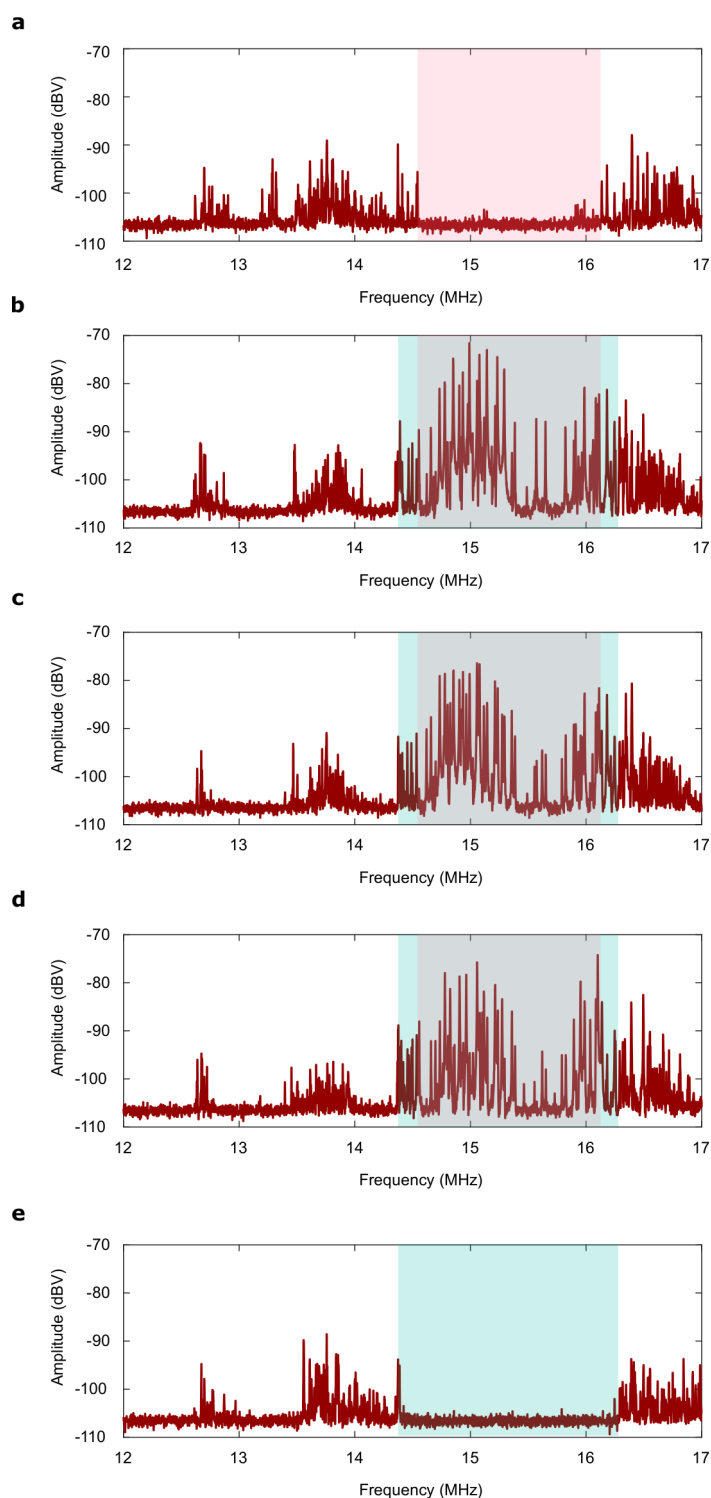
Extended Data Fig. 6 | Frequency responses of the NEMM with the pseudospin filter configuration. a–e, Frequency responses of the bulk of the non-trivial phase ($w = 6.5\,\mu m$; **a**), output 1 (**b**), output 2 (**c**), output 3 (**d**) and the bulk of the trivial phase ($w = 5.5\,\mu m$; **e**), shown in Fig. 4a. The light-red and light-blue regions represent the bandgaps of the non-trivial and trivial phases, respectively.